Annular Apertures in Metallic Screens as Extraordinary Transmission and Frequency Selective Surface Structures

Pablo Rodríguez-Ulibarri, Miguel Navarro-Cía, *Senior Member, IEEE*, Raúl Rodríguez-Berral, Francisco Mesa, *Fellow, IEEE*, Francisco Medina, *Fellow, IEEE*, and Miguel Beruete

***Abstract*— A 2-D periodic array of annular apertures (or ring slots) is studied using an accurate circuit model. The model accounts for distributed and dynamic effects associated with the excitation of high-order modes operating above or below cutoff but not far from their cutoff frequencies. This paper allows to ascertain the substantial differences of the underlying physics when this structure operates as a classical frequency selective surface or in the extraordinary-transmission (ET) regime. A discussion of two different designs working at each regime is provided by means of the equivalent circuit approach (ECA), full wave simulation results, and experimental characterization. The agreement between the equivalent circuit calculation applied here and the simulation and experimental results is very good in all the considered cases. This validates the ECA as an efficient minimal-order model and a low computational-cost design tool for frequency selective surfaces and ET-based devices. Additional scenarios such as oblique incidence and parametric studies of the structural geometry are also considered.**

***Index Terms*— Annular aperture, equivalent circuit, extraordinary transmission (ET), frequency selective surfaces (FSSs), millimeter waves, ring slot.**

I. Introduction

EXTRAORDINARY transmission (ET) has been a widely studied phenomenon in the last two decades. In 1998, T. W. Ebbesen *et al.* [1] published a seminal paper describing high-transmission peaks in perforated plates in the optical regime. Before [1], Betzig *et al.* [2] had observed similar peaks in metallic plates periodically perforated with subwavelength holes and had found a relation between these peaks and the excitation of surface plasmons, although they did not go as deeply as [1] into the underlying physics. These ET peaks were considered *extraordinary* because they appear well below the cutoff frequency of the apertures and still below the first Rayleigh–Wood (RW) anomaly [3], [4] (a deep null in the transmission spectrum related to the periodicity of the structure due to the onset of the first diffraction order). Ebbesen *et al.* [1] explained ET as the coupling of the incident light to surface plasmons polaritons (SPP); i.e., a type of surface waves sustained by a metal-dielectric interface at optical frequencies. This discovery gave a strong impulse to the scientific discipline termed plasmonics, leading ultimately to the so-called "plasmon resurrection" in the early years of the twenty-first century [6]. ET phenomenon has been widely used in optics and plasmonics for focusing, sensing, and near-field applications [7]. In addition, it has also been exploited within the field of antennas for achieving directive beams with subwavelength apertures [8].

When a new physical phenomenon is reported, some time is needed to fully understand the underlying physics. In ET, the first source of controversy was the exact role played by SPPs in the phenomenon. Remarkably, ET was also observed all along the electromagnetic spectrum including millimeter waves [9], where metals are modeled as high and real conductivity materials that do not support SPPs. A more general theory to explain ET was then developed based on the excitation of complex surface waves in the periodic structure, which in the case of optical frequencies coincide with leaky SPPs [10]–[12]. Following similar lines, equivalent circuits were crucial to give a deep insight into the underlying physics and have now become a fast analytical tool for the design and analysis of ET structures.

The first equivalent circuit for ET was discussed in [13]. There, the periodic problem was reduced to a single unit cell defined by a diaphragm located inside a virtual waveguide, and the ET peaks were explained in terms of the reactive elements accounting for the high-order modes scattered by the diaphragm. A more elaborated equivalent circuit approach (ECA) was later proposed in [14]. It was noticed that this ECA can also be applied to more classical periodic structures like frequency selective surfaces (FSSs), discussed

Manuscript received March 24, 2017; revised June 11, 2017; accepted July 1, 2017. This work was supported in part by the Spanish Ministerio de Economía y Competitividad with the European Union FEDER funds under Project TEC2013-41913-P and Project TEC2014-51902-C2-2-R and in part by the Spanish Junta de Andalucía under Project P12-TIC-1435. The work of P. Rodríguez-Ulibarri was supported by the Universidad Pública de Navarra under a Pre-Doctoral Scholarship. The work of M. Navarro-Cía was supported by the University of Birmingham under the Birmingham Fellowship. *(Corresponding author: Miguel Beruete.)*

P. Rodríguez-Ulibarri is with the Antennas Group-TERALAB, Department of Electrical and Electronic Engineering, Universidad Pública de Navarra, 31006 Pamplona, Spain (e-mail: pablo.rodriguez@unavarra.es).

M. Navarro-Cía is with the School of Physics and Astronomy, University of Birmingham, Birmingham B15 2TT, U.K. (e-mail: m.navarro-cia@bham.ac.uk).

R. Rodríguez-Berral and F. Mesa are with the Microwaves Group, Department of Applied Physics 1, ETS de Ingeniería Informática, Universidad de Seville, 41012 Seville, Spain (e-mail: rrberral@us.es; mesa@us.es).

F. Medina is with the Microwaves Group, Department of Electronics and Electromagnetism, Faculty of Physics, Universidad de Seville, 41012 Seville, Spain (e-mail: medina@us.es).

M. Beruete is with the Antennas Group-TERALAB, Department of Electrical and Electronic Engineering, and the Institute of Smart Cities, Universidad Pública de Navarra, 31006 Pamplona, Spain (e-mail: miguel.beruete@unavarra.es).

Color versions of one or more of the figures in this paper are available online at http://ieeexplore.ieee.org.

Digital Object Identifier 10.1109/TMTT.2017.2732985

below. In fact, FSSs have been historically studied by equivalent circuit techniques well before the appearance of ET phenomenon. Usually, circuit-model solutions were oriented toward reducing the electromagnetic problem to a simplified network of lumped elements (see [15]–[17]). Other works relied on multimodal equivalent networks in order to characterize planar strip gratings [18]–[20]. Recently, fully analytical ECAs have been derived by some of the authors of this paper for one-dimensional (1-D) and two-dimensional (2-D) periodic metallic screens printed on dielectric slabs [21], [22], stacked fishnet structures [23], or T-shaped corrugated surfaces [24]. A large number of papers dealing with equivalent circuits applied to FSS structures can be found elsewhere; see, for instance, the review presented in [25] and references therein.

Another source of controversy concerning ET has been how to delimit exactly what ET is and what it is not. Due to their similarity, ET resonances have sometimes been identified as standard resonances of FSSs. These are 2-D-periodic arrays of metallic patches (or apertures in metallic screens) that present a stopband (passband) associated with the resonance of the patch (aperture) [26]. It should be noted that even with a single patch (aperture), high reflection dips (transmission peaks) can be obtained due to self-resonances of the element. The addition of more elements in a periodic array affects mainly the amplitude of the transmittance and the bandwidth of the stopband/passband. In contrast, genuine ET peaks appear well below the cutoff frequency of the aperture and are associated with the excess of energy accumulated by the first diffraction order mode of the periodic structure as it approaches the onset from evanescent to propagating. This means that ET is a resonance related to the periodic nature of the structure rather than to the single element geometry itself. Therefore, a necessary condition for ET is that the aperture of the metallic screen has to be in cutoff. Although ET phenomena can also be observed in nonperiodic structures (such as diaphragms on circular waveguides [14], [27]), periodic structures are the most typical geometry analyzed in the literature, with their lattice size being of utmost importance.

The structure under study in this paper has a similar geometry as the coaxial hole arrays lately studied in the optical regime in the framework of ET [28]–[38]. In some of these works, high-transmission peaks observed in the spectrum were labeled as ET, although a more careful scrutiny demonstrates that they are associated with a resonance of the coaxial aperture; i.e., they appear at the cutoff frequency of the TE_{11} mode of the coaxial line. From our previous discussion, it is apparent that this peak should not be called ET. Following this formalism, Orbons and Roberts [32] correctly set the boundaries between FSS and ET regimes. In addition, Lomakin *et al.* [39] studied wave guiding across subwavelength coaxial metallic holes at the microwave and terahertz regimes.

In this paper, we use an ECA [22] that models and analyzes annular apertures (also called ring slots) drilled on a metallic screen to explore when the observed peaks correspond to ET excitation. As it was done in [22] for a different structure, the equivalent circuit topology is derived from very first principles giving rise to a fully analytical method with low computational cost, which additionally provides a comprehensive understanding of the underlying physics of the considered phenomena. The annular geometry studied here along with the perspective provided by the ECA allows for an easy identification of the ET or FSS regime in terms of its structural parameters. In most practical situations concerning FSS and ET structures, a dielectric substrate is required as mechanical support of the patterned metallic screen. Therefore, knowing the effect of this dielectric slab on the spectral response is very relevant for design purposes. Somehow naively, one may just take the behavior of a free standing FSS/ET structure and only expect a downshift of the resonance frequency due to the presence of the dielectric slab. However, a layered dielectric medium gives rise to additional features that need be taken into account [40], [41]. In fact, the response of a dielectric-backed FSS/ET structure may be relatively complex, especially in the frequency range selected here (millimeter waves) where the available commercial substrates can be considered electrically thick. The transmission/reflection results may show complex details because of multiple resonances occurring inside the dielectric slab. All these features are accurately modelled by the equivalent circuit developed in this paper.

This paper is organized as follows. Section II presents the analyzed geometry as well as an outline of the equivalent circuit employed (more details are given in the Appendix). Section III deals with the analytical and numerical comparison of cases selected to highlight the differences between FSS and ET regimes. Besides, several parametric studies of the structural parameters are presented. In Section IV, experimental results at millimeter waves are presented under both normal and oblique incidence. Finally, a summary of the main ideas discussed in this paper is given in Section V.

II. Geometry and Equivalent Circuit Approach Basics

The structure under consideration in this paper is a periodic array of annular apertures in a metallic screen. Both free standing and a dielectric slab backed structures are studied. Since the latter structures are more interesting for practical applications, a greater emphasis is put on them. The structure backed with dielectric slab along with its top and side views is shown in Fig. 1. The geometrical parameters of the unit cell are the internal radius a, external radius b, periodicity along x and y directions, d_x and d_y, respectively, and the dielectric substrate height h_s. Rectangular unit cells ($d_x \neq d_y$) are also used in order to distinguish between vertical and horizontal polarization and discern the different mechanisms involved in the transmission spectrum.

Given the periodic nature of the problem under consideration, Floquet analysis is employed (a time convention of the type $e^{j\omega t}$ is assumed throughout this paper). With this formalism, depending on the polarization and incidence angle of the impinging wave, the infinitely periodic problem is reduced to a generalized waveguide problem in which the boundary conditions can be either periodic, electric, or magnetic walls [13], [21]. The assumed field in the aperture can be expanded in terms of Floquet modes leading to a multimodal network equivalent circuit model wherein the

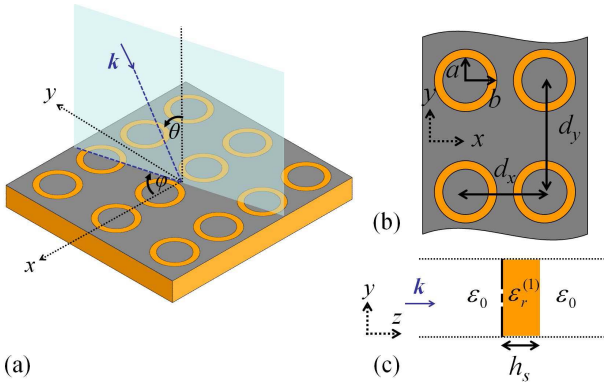

Fig. 1. (a) 2-D periodic structure with a rectangular array of annular apertures on a metallic screen backed with a dielectric slab. (b) Top view of a portion of the array structure. (c) Side view of a single unit cell.

harmonics are represented by transmission lines connected in parallel with associated coupling coefficients [22]. These coupling coefficients can be interpreted as turn ratio values of standard transformers, N_h. The field expansion in terms of Floquet modes is equivalent to evaluating the corresponding Fourier transform of the field profile at the aperture. The value of N_h can be calculated as the following dot product of the Fourier transform of the assumed field at the aperture, $\widetilde{\mathbf{E}}_a$, and the corresponding unit transverse wavevector ($\hat{\mathbf{k}}_{t,h}$ for TM harmonics or its cross-product with the unit vector $\hat{\mathbf{z}}$ for TE harmonics):

$$N_h = \begin{cases} \widetilde{\mathbf{E}}_a \cdot \left(\hat{\mathbf{k}}_{t,h} \times \hat{\mathbf{z}}\right), & \text{TE harmonics} \\ \widetilde{\mathbf{E}}_a \cdot \hat{\mathbf{k}}_{t,h}, & \text{TM harmonics.} \end{cases} \tag{1}$$

To achieve congruent and accurate results, the assumed field profile at the aperture has to be consistent with the aperture itself, the excitation, and the boundaries of the unit cell problem. Based on the previous experience of some of the authors of this paper, for normal incidence and geometrically simple apertures, it is sufficient to set the aperture field profile as the first propagating mode of the equivalent hollow waveguide. Two modes would be required for more complex situations, appearing in our case when oblique incidence is considered [42].

For a normally incident plane wave scenario (with electric field parallel to y axis), the original periodic problem can be reduced to the scattering of an aperture discontinuity inside a virtual waveguide with perfect electric top and bottom walls and perfect magnetic sidewalls. Given the polarization of the impinging wave, the first waveguide mode that can be excited in the annular aperture is the TE_{11}. It should be noticed that the symmetry of the incident wave precludes the excitation of any mode with even parity. Then, since the fundamental TEM mode cannot be excited, the TE_{11} is the mode with odd parity of lowest order to be considered. Thus, the first guess for the aperture field profile should resemble the field distribution of the TE_{11} coaxial mode. With these prescriptions, Dubrovka *et al.* [43] proposed a field aperture with only radial component and an angular dependence with a sine/cosine function. It should be taken into account that this approximation works as long as the slot width is sufficiently small ($b/a \approx 1$). As a further simplification, the angular component $\hat{\boldsymbol{\phi}}$ can be neglected and the radial component can be taken constant, independent on the radial distance (for larger b/a values, the $1/\rho$ dependence of the radial component should be taken into account). As our main purpose is to study the different FSS and ET operation regimes, we will apply this simplification in the following analysis. Therefore, we take the following aperture field profile [43]:

$$\mathbf{E}_a = A \cos\left(\varphi - \varphi_0\right)\hat{\boldsymbol{\rho}} \tag{2}$$

where A is a constant, φ is the azimuth angle, and φ_0 is the reference azimuth angle.

The problem of oblique incidence over an array of annular apertures has already been studied in [44]. In that work, the TEM mode field distribution is incorporated into the field profile of the aperture as a constant without neither radial nor angular dependence as

$$\mathbf{E}_a^{\mathrm{TEM}} = B\hat{\boldsymbol{\rho}} \tag{3}$$

where B is a constant. It should be noticed that the TEM mode can be uniquely excited under TM polarization for symmetry reasons.

Since the ECA used here is largely based on the approaches presented in [22] and [42]–[44], the explicit equations and circuit topologies are presented in the Appendix for completeness. Nevertheless it is worth noting that the contribution of the higher order modes is now incorporated in a distributed manner oppositely to the techniques employed in [43], where the authors restricted the analysis to lumped elements.

III. Analytical and Numerical Results

In this section, numerical and analytical results of the structure depicted in Fig. 1 are compared for different design configurations. First, a selected range of examples are studied to validate our ECA results in different scenarios. Next, two studies of a free-standing array of annular apertures are conducted to delimit and observe both FSS and ET operation regimes. In the first study, the mean radius of the aperture is varied while keeping the rest of parameters constant and, in the second one, the lattice period is swept while the aperture remains unchanged. In addition, two different dielectric backed designs are studied with geometrical parameters conveniently chosen to have either classical FSS or ET performance. It will be found that the ECA is able to accurately predict the response of structures working at different physical regimes.

A. Equivalent Circuit: General Results

Some particular free-standing structures with square unit cell ($d_x = d_y$) and several internal radii a, and dielectric backed substrates with different heights, h_s, and relative permittivity ε_r are analyzed by means of equivalent circuits and full wave simulations (see Fig. 2), assuming a normally incident plane wave. The frequency is normalized to the diffraction limit $f_{\mathrm{diff}} = c_0/d$, with d being the larger lattice period. The numerical results are computed using the full wave commercial software CST MICROWAVE STUDIO. For the

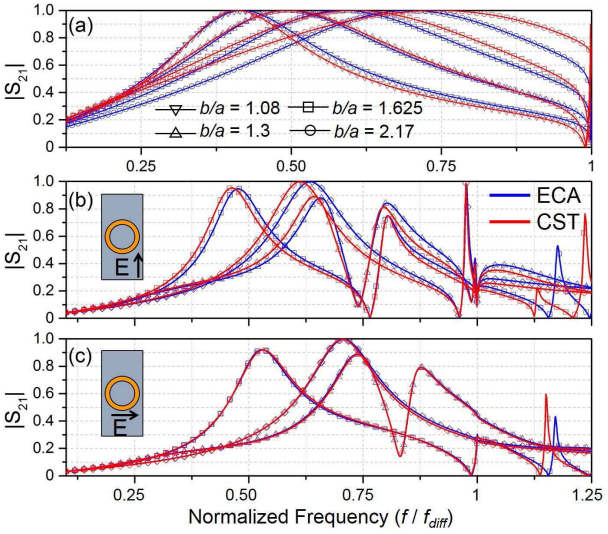

Fig. 2. Transmission coefficient results obtained by ECA (blue line) and CST (red line). Free standing structure: (a) $d_x = d_y = 1.5$ mm; $b = 0.65$ mm; $h_s = 0$ mm, and several internal radii from $a = 0.3$ to 0.6 mm. Dielectric backed structure: $d_x = 1.5$ mm; $d_y = 3$ mm; $b = 0.65$ mm; $a = 0.5$ mm; [□] $\varepsilon_r = 5$, $h_s = 0.4$ mm; [◇] $\varepsilon_r = 3$, $h_s = 0.2$ mm; [△] $\varepsilon_r = 2.1 - j0.018$, $h_s = 1.6$ mm. (b) Vertical polarization ($\varphi = 90°$). (c) Horizontal polarization ($\varphi = 90°$).

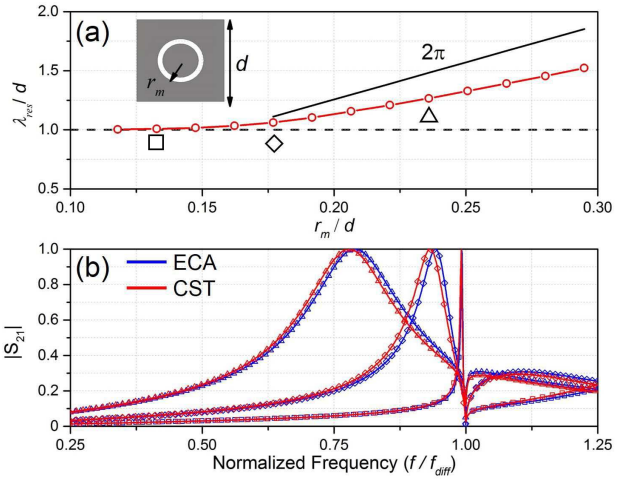

Fig. 3. (a) Resonant wavelength λ_{res} versus mean radius (r_m) normalized to the lattice period d for free-standing array of annular apertures with $b/a = 1.3$ and $d = 1.5$ mm. (b) Transmission coefficient results obtained by ECA (blue line) and CST (red line). [□] $b = 0.25$ mm ($r_m = 0.13d$ mm). [◇] $b = 0.3$ mm ($r_m = 0.177d$ mm). [△] $b = 0.4$ mm ($r_m = 0.236d$ mm).

simulation settings, the unit cell option is selected in the CST boundary conditions for the frequency domain solver. The metallic screen is made of perfect electric conductor with infinitesimal thickness. A tetrahedral mesh with adaptive refinement is selected with a maximum of eight steps and a stop criterion of 0.02 as threshold for consecutive absolute values of S-parameters. The stop criterion for the frequency sweep is again selected with respect to the absolute value of the S-parameters difference between consecutive calculations and set to 0.01.

Fig. 2(a) shows the results for the free standing structure. It can be seen that the accuracy of the circuit model is better for narrow slots ($b/a \approx 1$), in concordance with the assumed approximation that the field dependence with the radial distance is neglected. In any case, the agreement is quite good until $b/a \approx 1.5$. Results for dielectric-backed structures are shown in Fig. 2(b) and (c). In this case, the unit cell is rectangular leading to a polarization-dependent structure. Panels (b) and (c) show the response under vertical and horizontal polarization, respectively. It can be observed that the agreement is good in both the cases, with a better agreement for the horizontal polarization. Different dielectric slabs have been tested with similar level of agreement between ECA and CST results (note that dielectric loss can be easily modeled by setting the permittivity as a complex number). In all the analyzed cases, the computation resources used by the ECA are negligible in comparison with full wave simulations. For instance, for the cases selected in this section, a 2000-point frequency sweep is run within 1 or 2 s while the simulation may last several minutes. Certainly, this difference becomes even more crucial when parametric sweeps and optimization of the structure is required.

B. Discerning FSS and ET Regimes

In this section, our goal is to explore the limits between FSS and ET operation regimes. To this end, a square free-standing array of annular apertures is analyzed, keeping constant the b/a ratio and the period, d, ($b/a = 1.3$ and $d = 1.5$ mm, respectively) while the mean radius, $r_m = (a + b)/2$, is varied. The resonance wavelength, λ_{res}, is defined as the wavelength where the maximum transmission is obtained. This resonance wavelength (normalized to the lattice period) is plotted versus r_m/d in Fig. 3(a). It can be observed that for small radii ($0.1 < r_m/d < 0.15$), λ_{res} is practically equal to d regardless the aperture size. ET phenomenon can be claimed within this operation range. In contrast, for large r_m values ($r_m/d > 0.2$), λ_{res} is linearly proportional to the aperture size, which is the classical behavior expected for FSS regime. Between these two regions, there is a range ($0.15 < r_m/d < 0.2$), wherein λ_{res}/d is neither equal to 1 nor proportional to r_m/d, that can be considered as the boundary between FSS and ET regimes. Fig. 3(b) shows the transmission results obtained by the ECA and CST for three selected cases marked with symbols in Fig. 3(a): ET ($r_m = 0.2$ mm), FSS ($r_m = 0.35$ mm), and an intermediate case ($r_m = 0.265$ mm). Note that ET transmission peaks are inherently narrowband while FSS peaks are relatively wide.

Next, a rectangular ($d_x \neq d_y$) free-standing array of annular apertures is studied in order to evaluate the influence of the lattice period, d_y, in the transmission properties and the operation regime (FSS or ET). The remaining parameters are set to $d_x = 1.5$ mm, $b = 0.65$ mm, and $a = 0.5$ mm. With these dimensions, the cutoff frequency of the aperture is $f_{\text{ap}} = c_0/[(a + b)\pi] = 83.18$ GHz. The results for vertical and horizontal polarization are shown in Fig. 4(a) and (b), respectively. The figures also include white dashed lines marking f_{ap} as well as the limits of the FSS/ET regimes. Fig. 4(a) shows that, for vertical polarization, the transmission peak shifts to lower frequencies as d_y increases. It is also

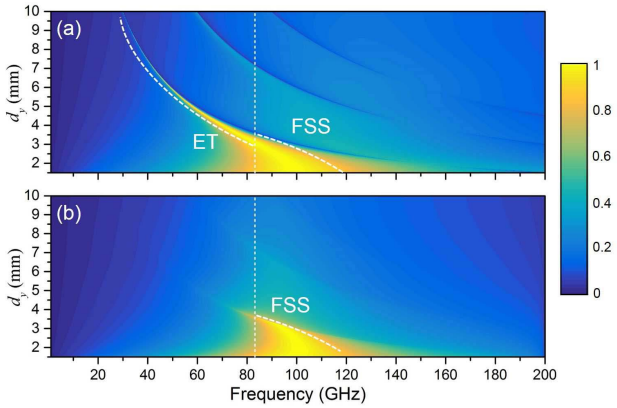

Fig. 4. ECA results of the transmission coefficient for FSS design versus frequency and d_y; $d_x = 1.5$ mm, $b = 0.65$ mm, and $a = 0.5$ mm. (a) Vertical polarization. (b) Horizontal polarization. Vertical white-dashed line accounts for the cutoff frequency aperture. The white-dashed curves delimit high transmission regions and hence, the ET and FSS regimes.

worth noting the appearance of high transmission bands below and above f_{ap} in the region 3 mm $< d_y <$ 3.5 mm. This corresponds to the aforementioned transition region where the high transmittance band is due to a combination of both FSS and ET regimes. When $d_y \approx 3.5$ mm the transmission above f_{ap} vanishes, and for $d_y > 3.5$ mm the high transmittance peak is completely due to the ET resonance. For the horizontal case in Fig. 4(b), it can be observed that ET does not take place, a fact that will be discussed later in this section. Thus, only the FSS region is highlighted in Fig. 4(b).

These results clearly set the boundaries between ET and FSS regimes. While the FSS regime is related to the aperture in the metallic screen and its exact location depends on its size and geometry, the ET peak always appears just before the first diffraction order, independently of the aperture geometry. In fact, for the FSS case, the high-transmission frequency is independent of the period and the transmission bands are broad. On the other hand, for ET, the frequency of the transmission peak is governed by the period and its bandwidth is always narrow.

In the next study we analyze structures printed on a dielectric slab, designed purposely to have either FSS or ET performance. These designs will be experimentally analyzed subsequently in Section IV. The geometrical parameters of the theoretical designed and final fabricated prototypes are outlined in Table I. Due to the dielectric slab loading, the cutoff frequency of the aperture is modified. Here, it is approximated as the cutoff frequency of the TE_{11} mode of the equivalent coaxial waveguide divided by the square root of the effective permittivity, ε_{eff} [45]

$$f_{\text{ap}} = \frac{c_0}{(a+b)\pi\sqrt{\varepsilon_{\text{eff}}}} \tag{4}$$

with c_0 being the speed of light in the vacuum. As it is well known, the magnitude of ε_{eff} depends on the surrounding media, with $1 < \varepsilon_{\text{eff}} < [\varepsilon_r^{(1)} + 1]/2$, where $\varepsilon_r^{(1)} = 2.4$ is the relative permittivity of the chosen dielectric slab. The exact value of ε_{eff} is not easy to estimate since it depends on the electrical dimensions of the dielectric slab and the metallic geometry. For simplicity, the upper-bound value of this parameter ($\varepsilon_{\text{eff}} = 1.7$) is taken for the evaluation of the f_{ap} values shown in Table I. It should be noted that the given f_{ap} then takes its lowest possible value.

TABLE I

GEOMETRICAL PARAMETERS OF THE STUDIED FSS/ET STRUCTURES ALONG WITH THE APERTURE CUTOFF FREQUENCY (f_{AP})

Design	a	b	d_x	d_y	h_s	$\varepsilon_r^{(1)}$	f_{ap} (GHz)
FSS	0.5	0.65	1.5	3	0.76	2.4	63.8
ET	0.3	0.5	1.5	5	0.76	2.4	91.6
FSS (prot.)	0.48	0.67	1.5	3	0.65	2.5	62.8
ET (prot.)	0.27	0.56	1.5	5	0.72	2.5	86.9

[1] dimensions are given in mm.

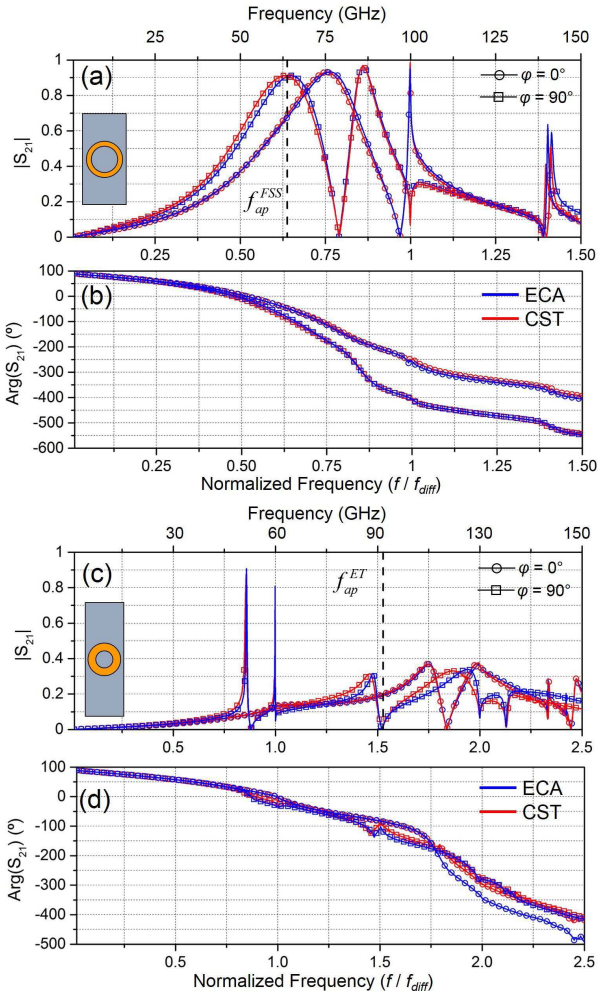

Fig. 5. Transmission coefficient for FSS and ET designs. ECA (blue line) and CST (red line) results are shown for vertical polarization ($\varphi = 90°$, squares) and horizontal polarization ($\varphi = 0°$, circles). (a) FSS—magnitude. (b) FSS—phase. (c) ET—magnitude. (d) ET—phase.

Fig. 5 shows a comparison between numerical and analytical results for the FSS and ET designs outlined in Table I. Normal incidence and both vertical and horizontal polarizations of the incident wave are considered. Magnitude and phase results are shown for the FSS [Fig. 5(a) and (b)] and ET [Fig. 5(c) and (d)] designs, respectively. To discern the nature of the

transmission peaks, the frequency is again normalized to the diffraction limit frequency, $f_{\text{diff}} = c_0/d_y$, for each case; i.e., 100 GHz for the FSS case and 60 GHz for the ET one. In addition, the aperture cutoff frequency for each design has been labeled in Fig. 5(a) and (c) as $f_{\text{ap}}^{\text{FSS}}$ and $f_{\text{ap}}^{\text{ET}}$, and marked with vertical dashed lines. As it can be seen, the agreement between CST simulation and ECA results is very good for both designs and polarizations, even above the diffraction limit ($f > f_{\text{diff}}$). For this reason, only the ECA will be used for analyzing the impact of the dielectric height, h_s, on the transmission features in both FSS and ET structures shown in Fig. 6 (the results are presented for both vertical and horizontal polarizations). The substrate thickness, h_s, was varied from 0 to 2 mm. The particular cases studied in Fig. 5 are depicted in Fig. 6 by means of horizontal white dashed lines.

For the vertical polarization case shown in Fig. 5(a), the first high transmission band of the FSS design appears near 65 GHz, near and slightly above $f_{\text{ap}}^{\text{FSS}} \approx 63.8$ GHz, and is located well below $f_{\text{diff}}^{\text{FSS}} \approx 100$ GHz. This transmission band precedes a null of transmission and a second transmission band that appear at 79 and 84 GHz, respectively. The null is due to the presence of the dielectric slab and can easily be explained with the ECA in terms of the first higher order mode of the equivalent virtual waveguide loaded with the dielectric medium with $\varepsilon_r^{(1)}$. In the present case, this role is played by the TM_{02} mode, whose cutoff frequency inside the dielectric is $f_{c,\text{TM}_{02}} = c_0/(d_y\sqrt{\varepsilon_r^{(1)}}) = 64.6$ GHz. The input admittance seen by TM_{02} diverges to infinity [pole in (12)] at a frequency that depends on the substrate characteristics and that is located between $f_{c,\text{TM}_{02}}$ and f_{diff}. Indeed, an admittance divergence is considered as a short-circuit in the ECA leading to a null of transmission that can be related to the RW anomaly inside the dielectric region [40]. As it can be seen in Fig. 6(a), when $h_s = 0$, a single transmission band is obtained but, as h_s increases, the null is shifted to lower frequencies, with its lower bound given by $f_{c,\text{TM}_{02}}$. It can be observed how the null appearance splits the transmission peak into two different transmission bands as h_s increases.

For the ET case and vertical polarization shown in Fig. 5(c), two transmission peaks arise at approximately 51 and 59.9 GHz, well below $f_{\text{ap}}^{\text{ET}} \approx 91.6$ GHz. The lower peak can be explained again by the the presence of the dielectric slab and the role of the TM_{02} mode of the equivalent virtual waveguide. The input admittance of the TM_{02} mode diverges to infinity leading to a null in the transmission spectrum at 52.8 GHz. Below this frequency, the total inductance due to the aperture can be compensated by the capacitance of the TM_{02} mode. For the second transmission peak, the situation is similar. In this case, it is due to the divergence of the TM_{02} admittance as it approaches propagation in the air [14]. Again, the TM_{02} mode contribution adds the required capacitance at a certain frequency near and below the first RW anomaly (60 GHz) to compensate the inductance introduced by the aperture. The particular origin of these two peaks can be better discerned when the substrate height, h_s, is varied [see Fig. 6(c)]. Two narrow-band transmission peaks arise between 45 and 60 GHz. The peak related to the dielectric

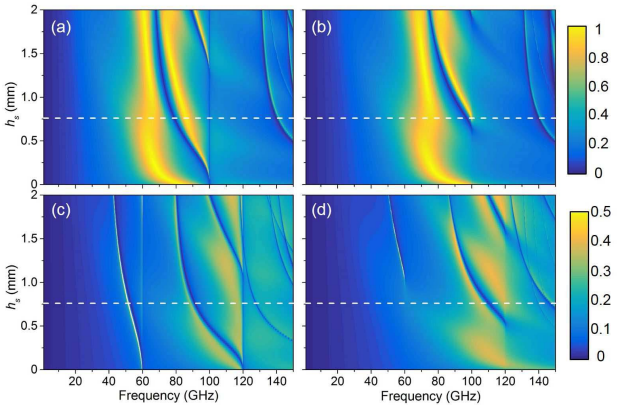

Fig. 6. ECA results of the transmission coefficient for FSS and ET designs versus frequency and h_s. (a) FSS—vertical polarization ($\varphi = 90°$). (b) FSS— horizontal polarization ($\varphi = 0°$). (c) ET—vertical polarization ($\varphi = 90°$). (d) ET—horizontal polarization ($\varphi = 0°$). Horizontal white dashed lines denote the particular cases shown in Fig. 5.

appears for $h_s > 0$ and shifts to lower frequencies as h_s increases. This shift finds its limit at approximately 45 GHz. On the other hand, as expected, the transmission peak related to the air region remains always just below the diffraction limit regardless the value of h_s. Furthermore, peaks with weak transmission arise within the diffraction regime between 90 and 120 GHz for the particular case shown in Fig. 5(c). These two low transmission peaks rely on the same principles as the ordinary transmission peaks of the FSS structure. In fact, they are broader than those obtained at 51 and 59.9 GHz, denoting that they are linked to the aperture resonance. Here, the transmission peak splits in two because of the divergence to infinity of a higher order mode (the TM_{04} mode in this case). This feature is corroborated by the results shown in Fig. 6(c) when the slab height, h_s, is swept. Indeed, the partial transmission arising at lower frequencies follows the trend of the null due to the dielectric. In any case, as these transmission peaks occur within the diffraction regime, part of the power is transferred to the diffraction modes and, hence, total transmission in the fundamental mode is not possible.

From these results, we can attribute to ET phenomena the two high and narrow transmission peaks arising at 51 and 59.9 GHz. Since there is an admittance that diverges to infinity in both cases, high-transmission peaks arise regardless the selected aperture geometry and size. Indeed, even for very small apertures in which very high capacitance is required to compensate small inductance values, the resonance condition is attainable due to the divergence to infinity [14]. It should be pointed out that in the ET case the inductance is low and therefore the quality factor, Q, is high. Hence, the transmission bands are inherently narrowband. On the other hand, for the FSS case, the inductance is usually large and the total capacitance required for resonance does not need to rely on singularities to attain the convenient value. Then, the transmission peaks obtained are broadband. Moreover, they can be regarded as ordinary because they are due to the resonance of the aperture.

In the case of horizontal polarization in Fig. 5(c), the results are quite different. Probably, the most remarkable difference comes from the absence of transmission peaks for the ET case within the nondiffractive regime. This can be explained again with the ECA. Now, due to the different polarization state, the first relevant high order mode is the TE_{02}. Below cutoff this mode is inductive, so its contribution is just adding an extra inductance and, therefore, the cancellation of the inductance due to the aperture does not seem possible. However, as explained in [46], with a proper selection of $\varepsilon_r^{(1)}$ and h_s, one could get an "anomalous" ET resonance [47], [48]. The condition for this phenomenon to occur is having $F = h_s[\varepsilon_r^{(1)} - 1]^{1/2}/d_y > 0.25$. In the case presented in Fig. 5(c), this is not satisfied given that $F = 0.18$. The only transmission feature that appears in the spectrum is an abrupt slope change at the first RW anomaly (60 GHz). Focusing now on the h_s study for this particular case [see Fig. 6(d)], it can be clearly seen this feature and how "anomalous" ET only occurs for sufficiently thick slabs, i.e., $F \approx 0.25$ ($h_s = 0.25d_y/(\sqrt{\varepsilon_r - 1}) \approx 1.05$ mm). The F parameter is linked to grounded slab configurations as detailed in [46]. As mentioned above, in this case, the first high order mode that becomes propagating inside the dielectric slab is the TE_{02}. Unlike the TM fundamental mode that propagates even with $h_s = 0$ [notice the null excursion from $h_s = 0$ and $f = 60$ GHz to $h_s = 2$ mm and $f \approx 40$ GHz in Fig. 6(c)], the fundamental TE mode requires a minimum h_s so that the transcendental modal equation has a valid solution [45]. In addition, a weak transmission peak is observed at approximately 105 GHz in Fig. 5(c). As in the vertical case, this transmission feature is due to the aperture resonance influenced by the TE_{04} mode dispersion. In fact, it can be observed in Fig. 6(c) that for thin substrates ($h_s < 0.5$ mm) a relatively broad and weak transmission band appears, reinforcing the argument about its connection with the aperture resonance. At the second RW anomaly frequency (120 GHz), a change in the slope of the transmission is again observed for all the h_s values. The rest of transmission features arising above 120 GHz and for slab heights $h_s > 1$ mm rely on the subsequent high order modes excitation, and then a further detailed discussion will not be addressed.

For the FSS design and horizontal polarization [Fig. 5(a)], a high-transmission band appears in the spectrum similar to the vertical polarization case but at a higher frequency (around 75 GHz). This transmission peak can again be directly linked to the annular aperture resonance, and its frequency shift with respect to the vertical polarization case can be attributed to the different contribution of the first higher order mode of the equivalent virtual waveguide. This contribution results in a different value of the effective permittivity; namely, ε_{eff} is higher for the vertical case than for the horizontal one. As ε_{eff} accounts for the static-capacitance variation due to the evanescent fields of cutoff TM modes, and these modes play a major role for the vertical polarization case than for the horizontal one, it leads to a higher value of ε_{eff} for the former polarization case. It is worth noting that TE modes at cutoff are inductive and are not affected by the surrounding medium [see (19)]. By inspecting Fig. 6(b) it is observed that, indeed, the differences in the performance are larger for thin substrates. As before, the first high order mode that becomes propagating inside the dielectric slab is the TE_{02} of the equivalent virtual waveguide. It can be observed that for thin substrates (up to $h_s = 0.65$ mm) a single band operation is retained while for higher h_s values the band is split in two. This is again directly connected to the F parameter presented before. In fact, $h_s = 0.25d_y/(\sqrt{\varepsilon_r - 1}) \approx 0.63$ mm. This feature can be tracked by observing the first null evolution in Fig. 6(b). It starts at $h_s \approx 0.65$ mm, $f = 100$ GHz and reaches a frequency of $f \approx 75$ GHz when $h_s = 2$ mm. In contrast, for the vertical polarization, a null excursion was observed from $h_s = 0$ and $f = 100$ GHz to $h_s = 2$ mm and $f \approx 70$ GHz [see Fig. 6(a)].

The results obtained in this section yield a quite complete understanding for accurately discerning between FSS and ET regimes. In addition, useful guidelines are given for practical design purposes where dielectric slabs are present. For instance, for the case of classical FSS design, if a single peak with nearly total transmission is required, thin substrates should be selected. For the studied case, within the range 0.5 mm $< h_s <$ 0.75 mm, a wider transmission band but with lower amplitude can be obtained. For larger h_s, double band solutions for both polarizations are possible. Similarly, for the ET case, the dependence of the high-transmission peak frequency location with h_s has been demonstrated. In addition, it should be mentioned that, despite the obvious differences between the geometrical parameters and the transmission spectra of the two studied designs, FSS and ET, the ECA results agree quite well with the full-wave simulation ones.

C. Oblique Incidence

The case of oblique incidence is briefly treated in this section. The structure under study is now the FSS design analyzed in Section III-B (the structural parameters can be found in Table I). Fig. 7 shows a comparison between simulation and ECA results when one and two modes in the aperture are considered under TM polarization. When only one mode is included, a single function compatible with the TE_{11} mode of the coaxial waveguide is used for approximating the field at the aperture. For the case of two modes, another function compatible with the TEM coaxial waveguide mode is added. A TM polarized wave with $\theta = 45°$ is considered for both principal incidence planes, $\varphi = 90°$ and $\varphi = 0°$. For the case when the incidence plane is parallel to the long period (d_y), it can be seen in Fig. 7(a) that the inclusion of the second mode slightly improves the accuracy of the equivalent circuit (specially in the prediction of the null at 55 GHz). For the orthogonal polarization shown in Fig. 7(b), the accuracy of the model at low frequencies is qualitatively improved when the contribution of the TEM mode is taken into account. In addition, the transmission peak observed after the null at approximately 95 GHz is much better predicted by the ECA considering two modes.

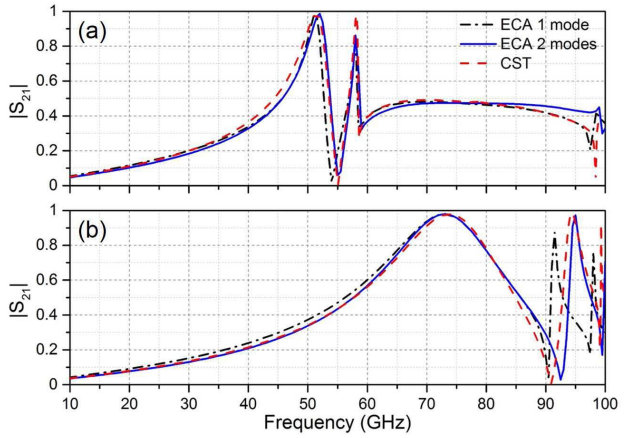

Fig. 7. Transmission coefficient results for the FSS design for TM polarized impinging wave and $\theta = 45°$. ECA with one mode in the aperture (black-dashed-dotted line), ECA with two modes (blue solid line), and CST (red dashed line) are shown. (a) $\varphi = 90°$. (b) $\varphi = 0°$.

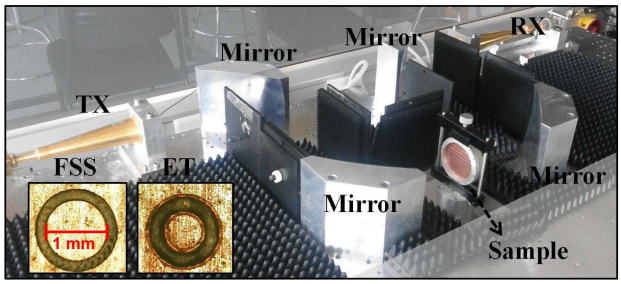

Fig. 8. Experimental setup. Insets: unit cell microscope picture of fabricated FSS and ET prototypes.

IV. Experimental Results

The numerical and analytical results obtained in the previous sections are corroborated here by experiments. To this end, two prototypes featuring the FSS and ET geometries considered in Section III-B were fabricated by milling machining. Microscope photographs of the unit cells of both fabricated prototypes can be found in the insets of Fig. 8. The selected commercial substrate was the ULTRALAM 2000 from Rogers Corp. The dielectric properties given by the manufacturer are the following (measured at 10 GHz): dielectric constant $2.4 \leq \varepsilon_r \leq 2.6$ and loss tangent $\tan\delta = 0.0022$. The thickness of the copper cladding is 35 μm. The measurements were made with an ABmm millimeter vector network analyzer equipped with a quasi-optical bench [49]. The experimental setup consists of two corrugated horn antennas [transmitter (TX) and receiver (RX)], four ellipsoidal mirrors to get a focused Gaussian beam illumination at the sample position, and an automatic rotatory platform where the sample is placed to perform oblique incidence measurements; a picture of the experimental setup is given in Fig. 8. The experimental characterization was carried out through a frequency sweep between 45 and 110 GHz in steps of 25 MHz. Two independent sets of TXs and RXs were employed to cover the V-band (45–75 GHz) and the W-band (70–110 GHz).

Fig. 9 shows a comparison between the obtained experimental and full-wave simulation results of the structure under

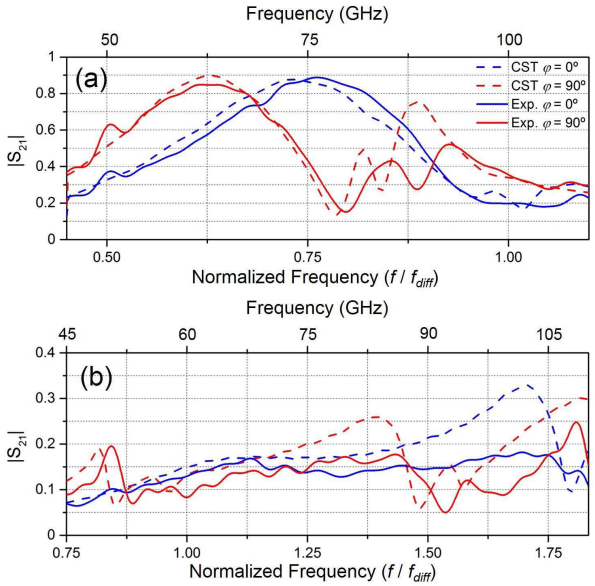

Fig. 9. Finite simulation and experimental results of fabricated samples for $\varphi = 0°$ and $\varphi = 90°$ incidence planes. (a) FSS prototype. (b) ET prototype.

normal incidence. The structural parameters of the fabricated prototypes differ slightly from those selected in the design section due to fabrication tolerances. The prototype parameters are shown in Table I, with these values being obtained from direct observation with a microscope. These are the parameters used in the CST full-wave simulation shown in Fig. 9. In addition, the dielectric permittivity is taken as $\varepsilon_r = 2.5$ and losses are included with a loss factor $\tan\delta = 0.006$. These values come from fitting with the experimental results and they are congruent with the values reported in the literature. In fact, dielectrics can show an increment of ε_r and $\tan\delta$ at frequencies ranging between millimeter and terahertz waves [50].

In order to achieve a reliable full-wave simulation of the actual finite structure, a Gaussian beam source and the time domain solver were chosen to model the experimental illumination. The Gaussian-beam field profile was set to have the focus exactly at the sample surface. The beam-waist diameter ($2w_0$) was 23 mm in agreement with the experimental value, so that it covers approximately half of the sample (the sample diameter is about 52 mm). The chosen frequency for the Gaussian beam definition was 75 GHz, roughly the center frequency of the range of interest. The finite simulation results correspond to the field recorded at a distance 45 mm away from the center of the prototype sample.

As it can be observed in Fig. 9, there is an overall acceptable agreement between experimental and simulation results. For the FSS structure [Fig. 9(a)], a good concordance is achieved for both incidence planes despite a small frequency downshift observed in the simulation. This disagreement can be attributed to either possible errors in the assumption of ε_r and h_s or the deficiency in modeling the frequency-dependent beamwaist of the Gaussian beam. In any case, the frequency shift is about 2.5% at 80 GHz. For the vertical polarization case (red lines), it can be observed that the second transmission band is seriously degraded in the experiment (red solid

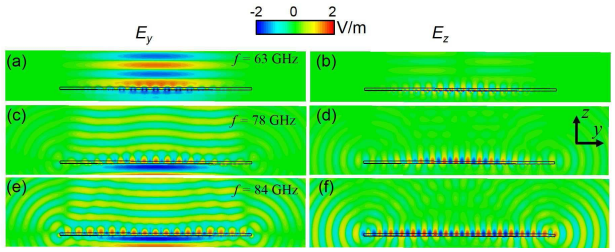

Fig. 10. Electric field distribution for the FSS design $\varphi = 0°$ incidence plane. (a) $E_y - f = 63$ GHz. (b) $E_z - f = 63$ GHz. (c) $E_y - f = 78$ GHz. (d) $E_z - f = 78$ GHz. (e) $E_y - f = 84$ GHz. (f) $E_z - f = 84$ GHz.

line). A transmission dip appears splitting the transmission peak in two. This phenomenon is also observed in the finite structure simulation (red dashed line). This feature is due to the nonuniformity of the wave that impinges onto the sample. Actually, due to the intrinsic propagation characteristics of the Gaussian beam, oblique wavevectors will be present at the illumination plane even under normal incidence. For this reason, the obtained response in this case shows the unfolding of the RW anomaly into two dips, as it would happen (and will be shown later) for oblique incidence under TM polarization and $\varphi = 90°$. To reinforce this argument, a field inspection of the full-wave simulation results for the FSS case at vertical polarization is presented in Fig. 10, where it is shown that the electric field distribution of the y and z components are at different frequencies, $f = 63$, 78, and 84 GHz. The yz-plane ($x = 0$) is chosen with the impinging wave propagating positively along the z axis. It can be seen that at 63 GHz the impinging wave is transmitted through the array with little reflections. The dominant field component is the vertical one [see Fig. 10(a) and (b)]. Conversely, a very high reflection appears at 78 and 84 GHz. In addition, waves running along the surface are observed at both frequencies (which are related to the RW anomaly unfolding), with a wave propagating along the surface eventually reaching the prototype edges and radiating at endfire. Another feature observed in both simulation and experimental results is a smoother RW anomaly compared to the one predicted by the ECA results shown in the previous section; a fact that can be directly related to the finite size of the fabricated samples [51] and the focused Gaussian beam illumination. For the horizontal polarization case [blue lines in Fig. 9(a)], the agreement is again good despite a slight frequency shift.

Regarding the ET design results shown in Fig. 9(b), it can be seen that the differences for the ET transmission peaks between simulations and measurements are greater than in the previous case. However, it should be noted that the major differences appear well inside the grating-lobe regime, a frequency region of less interest in this paper. Also, the discrepancies may appear overemphasized by the fact that the vertical-axis range in Fig. 9(b) is set from 0 to 0.4. The first transmission peak in this figure has lower amplitude than the one predicted by ECA results (see Fig. 5), and the second one disappears both in the simulations and measurements. The poor transmission at the first ET resonance as well as the vanishing of the second one can be attributed to an insufficient illumination of the annular apertures, as discussed in previous papers [52], [53]. In addition, these two resonances have a very high Q and thus losses strongly affect their transmission amplitude (as a lossy simulation not shown here has confirmed). It should be remarked that the aperture dimensions have been chosen to work deeply in the ET regime, so the apertures are very small compared to the wavelength resulting in an enhanced quality factor of the ET resonance [27]. The large differences above f_{diff} between the simulation and the measurements of the finite sample can be attributed to the grating-lobe contribution. In the finite simulation, the plane to record the field data was taken at a relatively short distance (45 mm) in order to make the problem computationally feasible (farther recording planes lead to computational requirements beyond the possibilities of our well-equipped workstation). However, at this relatively short distance, the energy associated with the grating lobes is still relevant for a wide range of frequencies and angular regions. In contrast, in the experimental measurements, the RX is placed at a much larger distance ($\sim$ 600 mm), preventing the detection of those grating lobes falling outside the narrow acceptance angle of the receiver.

Next, we study the oblique-incidence response for both prototypes. The rotatory platform is used for selecting the angle of incidence (θ_{in}) and, by switching the TX and RX antennas from vertical to horizontal position, TE and TM polarization can be selected. Finally, the rotation angle of the sample determines the plane of incidence; i.e., the alignment with $\varphi = 0°$ or $\varphi = 90°$ planes. The angular step is set to 5° and θ_{in} is swept from 0° to 45°. To fully characterize both prototypes, eight independent measurements were made in total (2 incidence planes $\times$ 2 polarizations (TE/TM) $\times$ 2 prototypes). For the sake of brevity, only results concerning TE incidence at $\varphi = 0°$ and TM incidence at $\varphi = 90°$ are shown for both FSS and ET designs in Figs. 11 and 12, respectively. In addition, CST simulation results of the infinite structure are shown. The computational effort required to characterize the oblique incidence is huge and, for a qualitative comparison, simulations of the infinite sample have been found sufficiently accurate. For completeness, ECA results are also included, and due to its low computational cost an angular step of 1° has been taken.

Regarding the FSS design in Fig. 11, an overall good agreement is obtained for the TE incidence at $\varphi = 0°$. The shift of the first null with increasing θ_{in} is clearly observed in the experiment [Fig. 11(a)]. As θ_{in} approaches 45°, the sample holder starts to block the impinging wave, resulting in a reduction of the transmitted power. For the ET case in Fig. 11, the differences are higher. As predicted in the finite-structure simulation presented in Fig. 9(b), the amplitude of the first ET peak is highly reduced and the second one (just before f_{diff}) vanishes. Thus, we have found some transmission features in the CST unit-cell simulation and ECA results [Fig. 11(d) and (f)] that are not present in the experimental results [Fig. 11(b)]. Despite this, the low transmission peak before the null located near 92 GHz is retained in the experiment.

For the case of TM polarization and $\varphi = 90°$ shown in Fig. 12, there is also a qualitative good agreement between the experiment, simulations, and ECA results. However, in this

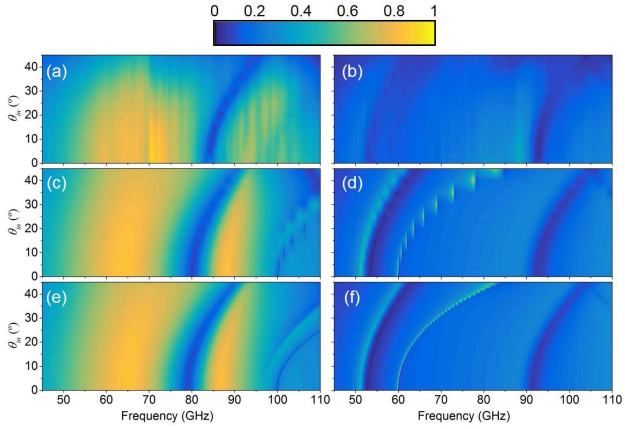

Fig. 11. Transmission coefficient versus frequency and θ_{in} for TE polarized impinging wave and $\varphi = 0°$ incidence plane for FSS and ET prototypes. (a) Experiment—FSS. (b) Experiment—ET. (c) CST—FSS. (d) CST—ET. (e) Equivalent circuit—FSS. (f) Equivalent circuit—ET.

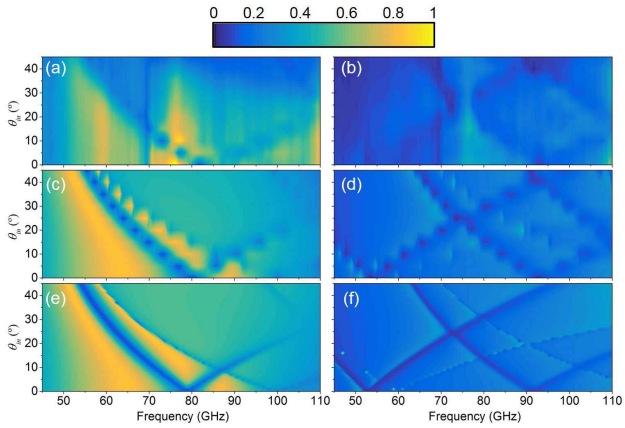

Fig. 12. Transmission coefficient versus frequency and θ_{in} for TM polarized impinging wave and $\varphi = 90°$ incidence plane for FSS and ET prototypes. (a) Experiment—FSS. (b) Experiment—ET. (c) CST—FSS. (d) CST—ET. (e) Equivalent circuit—FSS. (f) Equivalent circuit—ET.

case, an additional error source arises from the experimental setup since now the electric field emanating from the antenna is horizontally polarized. Although absorbent material is placed on the metallic bench, a ground effect on the measurements is hardly avoidable. In any case, for the FSS design [Fig. 12(a), (c), and (e)], the shift of the transmission band is retained in the experiment. Specifically, it is clearly observed the angle dependence of the dip that appears right after the transmission peaks. The discontinuities observed for the CST results [Fig. 12(c)] come from the angular step considered, and the subsequent interpolation. This artifact does not appear for the equivalent circuit model because of the smaller angular step taken. Regarding the ET design [Fig. 12(b), (d), and (f)], again very low transmission levels are obtained. Nevertheless, the experimental results still keep good agreement with the simulations and ECA results for the most important features. In fact, the "diamond-shape" regions delimited by the nulls are present in both simulations and experiments.

V. Conclusion

A 2-D periodic structure based on a metallic screen with annular apertures and backed with a dielectric substrate has been analyzed. The analysis includes free-standing structures and parametric studies of the lattice period and dielectric slab height. A special emphasis has been put on accurately setting the terminology when referring to structures having either a FSS or an ET operation regime. In this regard, two different designs working at different operation regimes (FSS and ET) have been studied by means of an ECA, full wave simulation, and experiments. In addition, it has been shown that the ECA accurately predicts the transmission features of this kind of structures regardless of the operation regime (FSS or ET). By some modifications of the ECA, oblique incidence has been tested as well.

A relevant result of the discussion on the FSS/ET operation regime is that ET phenomenon can only be claimed when the high-transmission peak is located well below the first resonance frequency of the aperture; otherwise, a typical FSS behavior is found. Our results and discussions have been sustained by the ECA providing a meaningful understanding of the underlying physics. In addition, the results of this approach are found to be very accurate regardless of the FSS/ET nature of the structure. Therefore, the ECA can be used as an efficient and time-saving analytical tool when compared with full-wave numerical solutions.

Regarding the experimental characterization, the obtained results corroborate the analytical and numerical findings. Despite the differences observed, the experimental results underscore the utility of the ECA as a design tool for FSS/ET structures as key elements in the development of devices such as spatial filters, dichroic filters, and polarizers.

Appendix

In this appendix, the explicit equations required to implement the ECA for normal and oblique incidence cases are provided.

A. Normal Incidence

Given the field aperture in (2), the following expressions for N_h are found [43]:

$$N_h^{\text{TE}} = 2\pi \frac{k_{\text{xn}} \sin(\varphi_0) + k_{\text{ym}} \cos(\varphi_0)}{k_{\rho,h}} \times \frac{-J_0(k_{\rho,h}b) + J_0(k_{\rho,h}a)}{k_{\rho,h}^2} \tag{5}$$

$$N_h^{\text{TM}} = 2\pi \frac{-k_{\text{xn}} \cos(\varphi_0) + k_{\text{ym}} \sin(\varphi_0)}{k_{\rho,h}} \times \frac{J_0(k_{\rho,h}b) - J_0(k_{\rho,h}a) + k_{\rho,h}[bJ_1(k_{\rho,h}b) - aJ_1(k_{\rho,h}a)]}{k_{\rho,h}^2} \tag{6}$$

with

$$k_{\text{xn}} = k_0 \sin\theta \cos\varphi + \frac{2\pi n}{d_x} \tag{7}$$

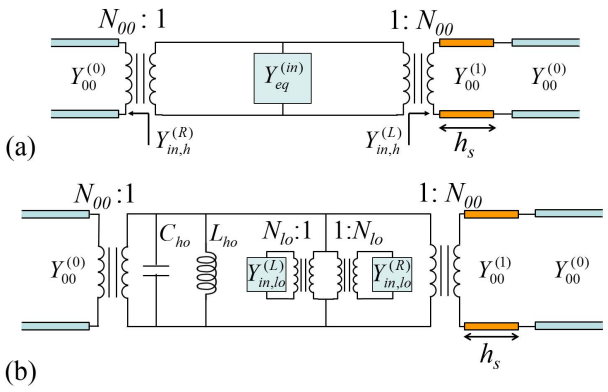

Fig. 13. (a) Equivalent network for a 00 impinging harmonic. (b) Equivalent network for 00 impinging harmonic in which the equivalent admittance is categorized into *lo* and *ho* modes.

$$k_{\mathrm{ym}} = k_0 \sin\theta \sin\varphi + \frac{2\pi m}{d_y} \tag{8}$$

$$k_{\rho,h} = |\mathbf{k}_{t,h}| = \sqrt{k_{\mathrm{xn}}^2 + k_{\mathrm{ym}}^2} \tag{9}$$

where k_0 is the vacuum wavenumber, h corresponds to a nm harmonic, $J_\nu(x)$ is the Bessel function of order ν, and argument x and θ and φ correspond to the elevation and azimuth angle, respectively. The inclusion of θ and φ allows us to present the equations in a general manner. For the particular case of normal incidence treated here, we simply set $\theta = 0°$ and $\varphi = 0°$ or $\varphi = 90°$. When $\theta \neq 0°$, the only modification that is required is to substitute the perfect electric or magnetic (depending on the polarization) walls of the virtual waveguide by periodic boundary conditions instead.

Now, the corresponding N_h turn ratios for TE and TM harmonics can be directly introduced into the equations governing the circuit in Fig. 13. The admittance in parallel labeled as $Y_{\mathrm{eq}}^{(\mathrm{in})}$ accounts for the infinite summation of the modal admittances of all the harmonics (both TM and TE) excluding the impinging mode (typically the $\mathrm{TE}_{00}/\mathrm{TM}_{00}$ mode). In this case, the parallel admittance, $Y_{\mathrm{eq}}^{(\mathrm{in})}$, can be written as the summation of the admittance for each h mode looking at the left, $Y_{\mathrm{in},h}^{(L)}$, and right, $Y_{\mathrm{in},h}^{(R)}$, sides of the circuit as follows:

$$Y_{\mathrm{eq}}^{(\mathrm{in})} = \sum_h |N_h|^2 \left[Y_{\mathrm{in},h}^{(L)} + Y_{\mathrm{in},h}^{(R)} \right] \tag{10}$$

where

$$Y_{\mathrm{in},h}^{(L)} = Y_h^{(0)} \tag{11}$$

$$Y_{\mathrm{in},h}^{(R)} = Y_h^{(1)} \frac{Y_h^{(0)} + jY_h^{(1)} \tan\left(\beta_h^{(1)} h_s\right)}{Y_h^{(1)} + jY_h^{(0)} \tan\left(\beta_h^{(1)} h_s\right)}. \tag{12}$$

Note that for a free standing structure $Y_{\mathrm{in},h}^{(R)} = Y_h^{(0)}$. The modal admittances $Y_h^{(i)}$ are given by

$$Y_h^{(i)} = \frac{1}{\eta^{(i)}} \begin{cases} \beta_h / k^{(i)}, & \text{TE harmonics} \\ k^{(i)} / \beta_h, & \text{TM harmonics} \end{cases} \tag{13}$$

where

$$k^{(i)} = \sqrt{\varepsilon_r^{(i)}} k_0 \tag{14}$$

$$\beta_h^{(i)} = \sqrt{\varepsilon_r^{(i)} k_0^2 - k_{\rho,h}^2} \tag{15}$$

$$\eta^{(i)} = \frac{\eta_0}{\sqrt{\varepsilon_r^{(i)}}} \tag{16}$$

with $\eta_0 = \sqrt{\mu_0/\varepsilon_0}$ being the vacuum wave impedance and $\varepsilon_r^{(i)}$ the relative permittivity of the medium (i). As explained in [22], a convenient distinction between low order (lo) and high order (ho) modes should be done. The former group, lo modes, are those in propagation (or evanescent but close to cutoff) at the frequency range of interest. Therefore, their explicit expression keeping their distributed nature (frequency dependent admittance) is taken. On the other hand, the contribution of high order TM/TE modes can be seen as regular capacitors/inductors, which are frequency independent. This fact allows us to save computational resources when performing a frequency sweep given that the circuit elements associated with high order modes are computed only once. It should be noted that the presence of a layered dielectric environment is explicitly taken into account for both low and high order modes [see Fig. 13(b)]. The final expression for the equivalent input admittance yields

$$Y_{\mathrm{eq}}^{(\mathrm{in})} = \sum_{|h| \leq M} |N_h|^2 \left[Y_{\mathrm{in},h}^{(L)} + Y_{\mathrm{in},h}^{(R)} \right] + j\omega C_{\mathrm{ho}} + \frac{1}{j\omega L_{\mathrm{ho}}} \tag{17}$$

with

$$C_{\mathrm{ho}} = \sum_{|h| \geq M+1}^{\infty} \left| N_h^{\mathrm{TM}} \right|^2 \times \left[\frac{\varepsilon_0}{k_{\rho,h}} + \frac{\varepsilon_0 \varepsilon_r^{(1)}}{k_{\rho,h}} \frac{\varepsilon_r^{(0)} + \varepsilon_r^{(1)} \tanh(k_{\rho,\mathrm{ho}} h_s)}{\varepsilon_r^{(1)} + \varepsilon_r^{(0)} \tanh(k_{\rho,\mathrm{ho}} h_s)} \right] \tag{18}$$

$$\frac{1}{L_{\mathrm{ho}}} = \sum_{|h| \geq M+1}^{\infty} \frac{2\mu_0 \left| N_h^{\mathrm{TE}} \right|^2}{k_{\rho,h}}. \tag{19}$$

As it can be seen from (17)–(19), the mode categorization is determined by the factor M which sets an upper limit for low order modes (in most practical cases M is a small integer number). In addition, the infinite series shown in (18) and (19) can be truncated by setting an upper bound N which fixes the maximum number of evanescent modes considered. Once all the circuital parameters are known, one may apply classical network theory to obtain the scattering parameters of the equivalent circuit [45].

B. Oblique Incidence

Provided the field profile in (3) that characterizes the TEM mode field distribution, the transformer turn ratios are given as follows [44]:

$$N_h^{\mathrm{TEM}} = j \frac{2\pi}{k_{\rho,h}^2} \left[\int_a^b J_0(k_{\rho,h}\rho)\, d\rho - k_{\rho,h} b J_0(k_{\rho,h} b) + k_{\rho,h} a J_0(k_{\rho,h} a) \right] \tag{20}$$

where the first integral term is evaluated in terms of Struve functions [54].

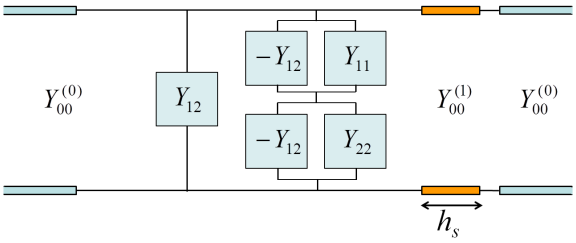

Fig. 14. Equivalent circuit model taking into account two independent spatial field profiles for characterizing oblique incidence under TM polarization.

The inclusion of an additional mode in the assumed aperture field profile leads to a different circuit topology than the one presented in the previous section. The equivalent circuit presented in Section V-A uses a single term for characterizing the field profile at the aperture. An ECA that takes an aperture field profile with two terms can be derived in order to enlarge the upper frequency bound of the model in metallic patch arrays and extend the approach to unit cell containing more than one scatterer [42]. This approach can also be applied to model the TM oblique incidence of a single annular aperture. One term characterizes the field profile of the TE_{11} mode and the other one the TEM mode. The corresponding equivalent circuit topology is shown in Fig. 14, where the Y_{11} and Y_{22} admittances account, respectively, for the first and second mode considered, and Y_{12} for the coupling between both modes. These admittances can be evaluated as

$$Y_{ij} = \sum_h \frac{N_{i,h}^* N_{j,h}}{N_{i,00}^* N_{j,00}} \left[Y_{\text{in},h}^{(L)} + Y_{\text{in},h}^{(R)} \right] \tag{21}$$

where $(i, j) = 1, 2$ and the same considerations outlined in Section A of this Appendix apply here (including the lo/ho mode distinction). Again, the scattering parameters can be evaluated by applying classical network theory.

REFERENCES

[1] T. W. Ebbesen, H. J. Lezec, H. F. Ghaemi, T. Thio, and P. A. Wolf, "Extraordinary optical transmission through sub-wavelength hole arrays," *Nature*, vol. 391, pp. 667–669, Feb. 1998.

[2] E. Betzig, A. Lewis, A. Harootunian, M. Isaacson, and E. Kratschmer, "Near field scanning optical microscopy (NSOM): Development and biophysical applications," *Biophys. J.*, vol. 49, no. 1, pp. 269–279, Jan. 1986.

[3] R. W. Wood, "On a remarkable case of uneven distribution of light in a diffraction grating spectrum," *Philos. Mag.*, vol. 4, no. 21, pp. 396–402, 1902.

[4] L. Rayleigh, "Note on the remarkable case of diffraction spectra described by Prof. Wood," *Philos. Mag.*, vol. 14, pp. 60–65, Jul. 1907.

[5] A. Ishimaru, *Electromagnetic Wave Propagation, Radiation, and Scattering*. Englewood Cliffs, NJ, USA: Prentice-Hall, 1991.

[6] S. A. Maier, *Plasmonics: Fundamentals and Applications*. New York, NY, USA: Springer, 2007.

[7] R. Gordon, A. G. Brolo, D. Sinton, and K. L. Kavanagh, "Resonant optical transmission through hole-arrays in metal films: Physics and applications," *Laser Photon. Rev.*, vol. 4, no. 2, pp. 311–335, 2010.

[8] H. J. Lezec *et al.*, "Beaming light from a subwavelength aperture," *Science*, vol. 297, no. 5582, pp. 820–822, Aug. 2002.

[9] M. Beruete *et al*, "Enhanced millimeter-wave transmission through subwavelength hole arrays," *Opt. Lett.*, vol. 29, no. 21, pp. 2500–2502, Nov. 2004.

[10] L. Martín-Moreno *et al.*, "Theory of extraordinary optical transmission through subwavelength hole arrays," *Phys. Rev. Lett.*, vol. 86, no. 6, p. 1114, Feb. 2001.

[11] D. R. Jackson, A. A. Oliner, T. Zhao, and J. T. Williams, "Beaming of light at broadside through a subwavelength hole: Leaky wave model and open stopband effect," *Radio Sci.*, vol. 40, no. 6, pp. 1–12, 2005.

[12] D. R. Jackson, J. Chen, R. Qiang, F. Capolino, and A. A. Oliner, "The role of leaky plasmon waves in the directive beaming of light through a subwavelength aperture," *Opt. Exp.*, vol. 16, no. 26, pp. 21271–21281, 2008.

[13] M. Beruete, I. Campillo, M. Navarro-Cía, F. Falcone, and M. S. Ayza, "Molding left- or right-handed metamaterials by stacked cutoff metallic hole arrays," *IEEE Trans. Antennas Propag.*, vol. 55, no. 6, pp. 1514–1521, Jun. 2007.

[14] F. Medina, F. Mesa, and R. Marqués, "Extraordinary transmission through arrays of electrically small holes from a circuit theory perspective," *IEEE Trans. Microw. Theory Techn.*, vol. 56, no. 12, pp. 3108–3120, Dec. 2008.

[15] R. J. Langley and A. J. Drinkwater, "Improved empirical model for the Jerusalem cross," *Proc. Inst. Elect. Eng.—Microw., Opt. Antennas*, vol. 129, no. 1, pt. H, pp. 1–6, Feb. 1982.

[16] R. J. Langley and E. A. Parker, "Double-square frequency-selective surfaces and their equivalent circuit," *Electron. Lett.*, vol. 19, no. 17, pp. 675–677, Aug. 1983.

[17] C. K. Lee and R. J. Langley, "Equivalent-circuit models for frequency-selective surfaces at oblique angles of incidence," *Proc. Inst. Elect. Eng.—Microw., Antennas Propag.*, vol. 132, no. 6, pt. H, pp. 395–399, Oct. 1985.

[18] I. Palocz and A. A. Oliner, "Equivalent network of a multimode planar grating," *IEEE Trans. Microw. Theory Techn.*, vol. MTT-18, no. 5, pp. 244–252, May 1970.

[19] M. Guglielmi and A. A. Oliner, "Multimode network description of a planar periodic metal-strip grating at a dielectric interface—Part II: Small-aperture and small-obstacle solutions," *IEEE Trans. Microw. Theory Techn.*, vol. 37, no. 3, pp. 542–552, Mar. 1989.

[20] M. Guglielmi and H. Hochstadt, "Multimode network description of a planar periodic metal-strip gratingat a dielectric interface—Part III: Rigorous solution," *IEEE Trans. Microw. Theory Techn.*, vol. 37, no. 5, pp. 902–909, May 1989.

[21] R. Rodríguez-Berral, C. Molero, F. Medina, and F. Mesa, "Analytical wideband model for strip/slit gratings loaded with dielectric slabs," *IEEE Trans. Microw. Theory Techn.*, vol. 60, no. 12, pp. 3908–3918, Dec. 2012.

[22] R. Rodríguez-Berral, F. Mesa, and F. Medina, "Analytical multimodal network approach for 2-D arrays of planar patches/apertures embedded in a layered medium," *IEEE Trans. Antennas Propag.*, vol. 63, no. 5, pp. 1969–1984, May 2015.

[23] V. Torres, F. Mesa, M. Navarro-Cía, R. Rodríguez-Berral, M. Beruete, and F. Medina, "Accurate circuit modeling of fishnet structures for negative-index-medium applications," *IEEE Trans. Microw. Theory Techn.*, vol. 64, no. 1, pp. 15–26, Jan. 2016.

[24] C. Molero, R. Rodríguez-Berral, F. Mesa, and F. Medina, "Analytical circuit model for 1-D periodic T-shaped corrugated surfaces," *IEEE Trans. Antennas Propag.*, vol. 62, no. 2, pp. 794–803, Feb. 2014.

[25] F. Costa, A. Monorchio, and G. Manara, "An overview of equivalent circuit modeling techniques of frequency selective surfaces and metasurfaces," *Appl. Comput. Electromagn. Soc. J.*, vol. 29, no. 12, pp. 960–976, 2014.

[26] B. A. Munk, *Frequency Selective Surfaces: Theory and Design*. New York, NY, USA: Intersci., 2000.

[27] F. Medina, F. Mesa, J. A. Ruíz-Cruz, J. M. Rebollar, and J. R. Montejo-Garai, "Study of extraordinary transmission in a circular waveguide system," *IEEE Trans. Microw. Theory Techn.*, vol. 58, no. 6, pp. 1532–1542, Jun. 2010.

[28] F. Baida and D. Van Labeke, "Light transmission by subwavelength annular aperture arrays in metallic films," *Opt. Commun.*, vol. 209, nos. 1–3, pp. 17–22, Jun. 2002.

[29] F. I. Baida and D. Van Labeke, "Three-dimensional structures for enhanced transmission through a metallic film: Annular aperture arrays," *Phys. Rev. B, Condens. Matter*, vol. 67, p. 155314, Apr. 2003.

[30] W. Fan, S. Zhang, B. Minhas, K. J. Malloy, and S. R. J. Brueck, "Enhanced infrared transmission through subwavelength coaxial metallic arrays," *Phys. Rev. Lett.*, vol. 94, Jan. 2005, Art. no. 033902.

[31] M. J. Lockyear, A. P. Hibbins, J. R. Sambles, and C. R. Lawrence, "Microwave transmission through a single subwavelength annular aperture in a metal plate," *Phys. Rev. Lett.*, vol. 94, May 2005, Art. no. 193902.

[32] S. M. Orbons and A. Roberts, "Resonance and extraordinary transmission in annular aperture arrays," *Opt. Exp.*, vol. 14, no. 26, pp. 12623–12628, Dec. 2006.

[33] S. M. Orbons *et al.*, "Extraordinary optical transmission with coaxial apertures," *Appl. Phys. Lett.*, vol. 90, no. 25, Jun. 2007, Art. no. 251107.
[34] F. I. Baida, Y. Poujet, J. Salvi, D. Van Labeke, and B. Guizal, "Extraordinary transmission beyond the cut-off through sub-λ annular aperture arrays," *Opt. Commun.*, vol. 282, no. 7, pp. 1463–1466, Jan. 2009.
[35] P. Banzer, J. Kindler, S. Quabis, U. Peschel, and G. Leuchs, "Extraordinary transmission through a single coaxial aperture in a thin metal film," *Opt. Exp.*, vol. 18, no. 10, pp. 10896–10904, May 2010.
[36] G. Si *et al.*, "Annular aperture array based color filter," *Appl. Phys. Lett.*, vol. 99, no. 3, Jul. 2011, Art. no. 033105.
[37] Z. Wei, J. Fu, Y. Cao, C. Wu, and H. Li, "The impact of local resonance on the enhanced transmission and dispersion of surface resonances," *Photon. Nanostruct. Fundam. Appl.*, vol. 8, no. 2, pp. 94–101, May 2010.
[38] Z. Wei, Y. Cao, Y. Fan, X. Yu, and H. Li, "Broadband transparency achieved with the stacked metallic multi-layers perforated with coaxial annular apertures," *Opt. Exp.*, vol. 19, no. 22, pp. 21425–21431, Oct. 2011.
[39] V. Lomakin, S. Li, and E. Michielssen, "Transmission through and wave guidance on metal plates perforated by periodic arrays of through-holes of subwavelength coaxial cross-section," *Microw. Opt. Technol. Lett.*, vol. 49, no. 7, pp. 1554–1558, Jul. 2007.
[40] R. J. Luebbers and B. A. Munk, "Some effects of dielectric loading on periodic slot arrays," *IEEE Trans. Antennas Propag.*, vol. AP-26, no. 4, pp. 536–542, Jul. 1978.
[41] P. Callaghan, E. A. Parker, and R. J. Langley, "Influence of supporting dielectric layers on the transmission properties of frequency selective surfaces," *Proc. Inst. Elect. Eng.—Microw., Antennas Propag.*, vol. 138, no. 5, pt. H, pp. 448–454, Oct. 1991.
[42] F. Mesa, R. Rodríguez-Berral, M. García-Vigueras, F. Medina, and J. R. Mosig, "Simplified modal expansion to analyze frequency-selective surfaces: An equivalent circuit approach," *IEEE Trans. Antennas Propag.*, vol. 64, no. 3, pp. 1106–1111, Mar. 2016.
[43] R. Dubrovka, J. Vazquez, C. Parini, and D. Moore, "Equivalent circuit method for analysis and synthesis of frequency selective surfaces," *Proc. Inst. Elect. Eng.—Microw., Antennas Propag.*, vol. 153, no. 3, pp. 213–220, Jun. 2006.
[44] R. Dubrovka, J. Vazquez, C. Parini, and D. Moore, "Multi-frequency and multi-layer frequency selective surface analysis using modal decomposition equivalent circuit method," *IET Microw., Antennas Propag.*, vol. 3, no. 3, pp. 492–500, Apr. 2009.
[45] D. M. Pozar, *Microwave Engineering*. New York, NY, USA: Wiley, 2009.
[46] M. Beruete, M. Navarro-Cía, and M. S. Ayza, "Understanding anomalous extraordinary transmission from equivalent circuit and grounded slab concepts," *IEEE Trans. Microw. Theory Techn.*, vol. 59, no. 9, pp. 2180–2188, Sep. 2011.
[47] V. Lomakin and E. Michielssen, "Enhanced transmission through metallic plates perforated by arrays of subwavelength holes and sandwiched between dielectric slabs," *Phys. Rev. B, Condens. Matter*, vol. 71, no. 23, 2005, Art. no. 235117.
[48] S. A. Kuznetsov *et al.*, "Regular and anomalous extraordinary optical transmission at the THz-gap," *Opt. Exp.*, vol. 17, no. 14, pp. 11730–11738, 2009.
[49] *AB Millimetre–Company Specialized in MVNA Manufacturing*. Accessed on Mar. 2017. [Online]. Available: http://www.abmillimetre.com
[50] S. Ramo, J. R. Whinnery, and T. Van Duzer, *Fields and Waves in Communication Electronics*. New York, NY, USA: Wiley, 1994.
[51] M. Camacho, R. R. Boix, and F. Medina, "Computationally efficient analysis of extraordinary optical transmission through infinite and truncated subwavelength hole arrays," *Phys. Rev. E, Stat. Phys. Plasmas Fluids Relat. Interdiscip. Top.*, vol. 93, no. 6, 2016, Art. no. 063312.
[52] M. Beruete, M. Sorolla, I. Campillo, and J. S. Dolado, "Increase of the transmission in cut-off metallic hole arrays," *IEEE Microw. Wireless Compon. Lett.*, vol. 15, no. 2, pp. 116–118, Feb. 2005.
[53] M. Beruete, M. Sorolla, M. Navarro-Cía, F. Falcone, I. Campillo, and V. Lomakin, "Extraordinary transmission and left-handed propagation in miniaturized stacks of doubly periodic subwavelength hole arrays," *Opt. Exp.*, vol. 15, no. 3, pp. 1107–1114, Feb. 2007.
[54] M. Abramowitz and I. Stegun, *Handbook of Mathematical Functions*. New York, NY, USA: Dover, 1970.

Pablo Rodríguez-Ulibarri was born in Pamplona, Spain, in 1986. He received the M.Sci. degree in telecommunication engineering and M.Res. degree in communications from the Universidad Pública de Navarra, Navarra, Spain, in 2010 and 2013, respectively, where he is currently pursuing the Ph.D. degree with the Antennas Group-TERALAB.

From 2011 to 2013, he was a Research Assistant with the Electrical and Electronic Engineering Department, Universidad Pública de Navarra. From 2013 to 2014, he was a Researcher with the Fraunhofer Institute of High Frequency and Radar, Wachtberg, Germany. He was a Visiting Researcher with the Universidad de Seville, Seville, Spain, in 2016. His current research interests include metamaterials, antennas, frequency-selective surfaces, and advanced devices ranging from microwave to terahertz frequencies.

Miguel Navarro-Cía (S'08–M'10–SM'15) was born in Pamplona, Spain, in 1982. He received the M.Sci. and Ph.D. degrees in telecommunication engineering, and M.Res. degree in introduction to research in communications from the Universidad Pública de Navarra, Navarra, Spain, in 2006, 2010, and 2007, respectively.

From 2006 to 2010, he was a Pre-Doctoral Researcher (FPI Fellowship recipient) with the Electrical and Electronic Engineering Department, Universidad Pública de Navarra, where he was a Research and Teaching Assistant from 2010 to 2011. He was a Research Associate with Imperial College London, London, U.K., in 2011 and at University College London, in 2012, and a Junior Research Fellow with Imperial College London, from 2012 to 2015. Currently, he is a Birmingham Fellow with the School of Physics and Astronomy, University of Birmingham, Birmingham, U.K. He is also affiliated as a Visiting Researcher with Imperial College London and University College London. He was a Visiting Researcher with the University of Pennsylvania, Philadelphia, PA, USA, for three months in 2010, with Imperial College London in 2008, 2009, and 2010 for four, six, and three months, respectively, and with the Valencia Nanophotonics Technology Center, Valencia, Spain, for two months in 2008. His current research interests include plasmonics, near-field time-domain spectroscopy/microscopy, metamaterials, and antennas and frequency-selective surfaces at millimeter-wave, terahertz, and infrared.

Dr. Navarro-Cía is a Senior Member of the Optical Society of America and a member of the Institute of Physics. He was a recipient of the Best Doctoral Thesis in Basic Principles and Technologies of Information and Communications, and Applications corresponding to the XXXI Edition of Awards "Telecommunication Engineers" 2010 and twice the CST University Publication Award for the best international journal publication using CST Microwave Studio (in 2012 and 2016). He was also a recipient of the 2011 Junior Research Raj Mittra Travel Grant.

Raúl Rodríguez-Berral was born in Casariche, Seville, Spain, in 1978. He received the M.Sc. (Licenciado) and Ph.D. degrees in physics from the University of Seville, Seville, in 2001 and 2008, respectively.

In 2002, he joined the Department of Applied Physics 1, University of Seville, where he is currently an Associate Professor. His current research interests include the study of the spectrum and the excitation of periodic and nonperiodic planar structures and high-frequency circuit modeling.

Francisco Mesa (M'93–SM'11–F'14) was born in Cádiz, Spain, in 1965. He received the Licenciado and Ph.D. degrees in physics from the Universidad de Seville, Seville, Spain, in 1989 and 1991, respectively.

He is currently a Professor with the Department of Applied Physics 1, Universidad de Seville. His current research interests include electromagnetic propagation/radiation in planar structures.

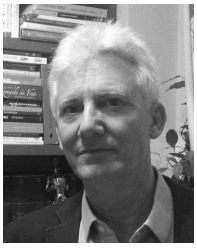

Francisco Medina (M'90–SM'01–F'10) was born in Puerto Real, Cádiz, Spain, in 1960. He received the Licenciado and Ph.D. degrees in physics from the University of Seville, Seville, Spain, in 1983 and 1987, respectively.

He is currently a Professor of electromagnetism with the Department of Electronics and Electromagnetism, University of Seville, where he was also the Head of the Microwaves Group. He has coauthored more than 130 journal papers and book chapters on those topics and more than 260 conference contributions. His current research interests include analytical and numerical methods for planar structures, anisotropic materials, and artificial media modeling.

Dr. Medina is a Reviewer for more than 40 IEEE, IET, AIP, and IOP journals and has been a member of the TPCs of a number of local and international conferences.

Miguel Beruete was born in Pamplona, Spain, in 1978. He received the M.Sci. and Ph.D. degrees in telecommunication engineering from the Public University of Navarre (UPNA), Navarre, Spain, in 2002 and 2006, respectively.

From 2002 to 2007, he was a Pre-Doctoral Researcher (FPI fellowship recipient) with the Electrical and Electronic Engineering Department, UPNA. In 2005, he was a Visiting Researcher with the University of Seville, Seville, Spain, as a part of his doctoral research. From 2007 to 2009, he was with the Electronics Department, Technological Center CEMITEC, Navarre, where he was involved in developing, designing, and measuring high-frequency communication devices. In 2009, he joined TERALAB, UPNA, as a Post-Doc Researcher on the Consolider EMET "Engineering Metamaterials" project. From 2012 to 2016 he was a Ramon y Cajal Fellow Researcher and subsequently he was upgraded to Distinguished Researcher. Since March 2017, he has been an Associate Professor with the Antennas Group-TERALAB, UPNA, where he supervises several Ph.D. and M.Sci. theses and leads the TERALAB Laboratory. He has authored more than 120 JCR articles, 4 book chapters, nearly 250 conference communications, and holds 3 patents. He is a Reviewer for more than 40 international journals. His current research interests include terahertz sensing and communication technology, including metamaterials, plasmonics, extraordinary transmission structures, leaky-wave antennas, nanoantennas, and in general quasi-optical devices.

Dr. Beruete was a recipient of the Ph.D. Prize from UPNA for the Best Doctoral Thesis in 2006–2007, three CST University Publication Awards for the best international journal publication using CST in 2005, 2012, and 2016, the XII Talgo Award of Technological Innovation in 2011, and several awards of international conferences.